Folding Propensity of Intrinsically Disordered Proteins by Osmotic Stress†

Amanda L. Mansouri[a], Laura N. Grese[a,b], Erica L. Rowe[a,b], James C. Pino[c], S. Chakra Chennubhotla[d], Arvind Ramanathan[c], Hugh M. O'Neill[b], Valerie Berthelier[a], and Christopher B. Stanley [b*]

Received Xth XXXXXXXXXX 2016, Accepted Xth XXXXXXXXX 2016
First published on the web Xth XXXXXXXXXX 2016
DOI: 10.1039/b000000x

Proteins imparted with intrinsic disorder conduct a range of essential cellular functions. To better understand the folding and hydration properties of intrinsically disordered proteins (IDPs), we used osmotic stress to induce conformational changes in nuclear co-activator binding domain (NCBD) and activator for thyroid hormone and retinoid receptor (ACTR) separate from their mutual binding. Osmotic stress was applied by the addition of small and polymeric osmolytes, where we discovered that water contributions to NCBD folding always exceeded those for ACTR. Both NCBD and ACTR were found to gain α-helical structure with increasing osmotic stress, consistent with their folding upon NCBD/ACTR complex formation. Using small-angle neutron scattering (SANS), we further characterized NCBD structural changes with the osmolyte ethylene glycol. Here a large reduction in overall size initially occurred before substantial secondary structural change. By focusing on folding propensity, and linked hydration changes, we uncover new insights that may be important for how IDP folding contributes to binding.

Introduction

The flexibility of intrinsically disordered proteins (IDPs) has shifted the classic structure-function view of proteins to include function arising from disorder.[1–3] IDPs often contain both unstructured and structured regions that work in concert. Existing as an ensemble in the unbound state, many IDPs undergo a disorder-to-order transition upon binding. The advantage is binding with high specificity but low affinity, which is desirable for signaling and other processes. IDPs serve numerous other roles, from linker regions to displaying post-translational modification sites.

Experiments and computations probing IDP ensembles[4–6] and folding-binding[7,8] have provided many important insights. Particular studies have investigated the response of IDPs to crowding conditions, which mimic the intracellular environment (see reviews[9,10]). Using crowding agents (osmolytes), like Ficoll, poly(ethylene glycol) (PEG), trimethylamine N-oxide (TMAO), or other proteins, observed effects on IDP structure range from pronounced folding and compaction[11–13] to essentially no change.[14–16] While osmolytes can act through various mechanisms,[17–19] they do provide a way to perturb IDP ensembles and understand their folding. The osmolyte-induced coil-to-helix transition in poly(glutamic acid) is a fundamental example that gave residue-level hydration changes.[20] Toward explaining experimental observations of IDP crowding, theoretical descriptions[13,21–23] and computational investigations[24,25] have resulted. These studies highlighted the impact of osmolyte size, size ratio between the IDP and osmolyte, and IDP-osmolyte interactions. Particularly relevant to our results are the theoretical order-disorder phase diagrams that incorporate IDP sequence dependence and solvent effects.[22]

Here we used osmotic stress to examine the folding and hydration properties of two IDPs, nuclear co-activator binding domain (NCBD) of CREB binding protein and activator for thyroid hormone and retinoid receptor (ACTR), in their unbound state. NCBD and ACTR are a well-studied IDP pair that form a tight 1:1 complex with synergistic folding upon binding.[7] The binding is enthalpically driven with hydrophobic burial at the interface.[26] NCBD maintains more α-helical content than ACTR in the free state, but experiments have detailed certain aspects of ACTR residual structure that likely are important for binding to NCBD.[27,28] The particular ACTR fragment used here, mouse ACTR(1025-1098), contains the

† Electronic Supplementary Information (ESI) available: See DOI: 10.1039/b000000x/

[a] *Department of Medicine, Graduate School of Medicine, University of Tennessee Health Science Center, Knoxville, TN, USA*
[b] *Biology and Soft Matter Division, Oak Ridge National Laboratory, Oak Ridge, TN, USA*
[c] *Health Data Sciences Institute, Computational Science and Engineering Division, Oak Ridge National Laboratory, Oak Ridge, TN, USA*
[d] *Department of Computational and Systems Biology, University of Pittsburgh, Pittsburgh, PA, USA*
Present Addresses: E.L. Rowe, School of Pharmacy, South College, Knoxville, TN and J. Pino, Vanderbilt University School of Medicine, Nashville, TN

47-residue NCBD-binding region and 27 additional sequence residues on the N-terminus. The additional N-terminal region contains an LXXLL motif.

With the osmotic stress method, we show how osmolyte effects are mediated through the waters that preferentially hydrate the molecular surfaces of these IDPs. We also demonstrate that osmolytes have a significant structural effect on the NCBD and ACTR conformational ensembles. In particular, the osmotic stress generated by both small and polymeric osmolytes favored increased α-helical content in the unbound form of these IDPs, consistent with the α-helix gain for each IDP upon forming the NBCD/ACTR complex.

Materials and Methods

Materials

The nuclear receptor co-activator binding domain (NCBD) of mouse cAMP response element binding (CREB) protein (CBP, accession: NP_001020603), CBP(2059-2117) (59 residues, 6545 Da) and the interaction domain of mouse activator for thyroid hormone and retinoid receptor (ACTR, accession: o09000), ACTR(1025-1098) (74 residues, 7989 Da) were synthesized by solid-phase FMOC chemistry (Keck-Yale facility). The crude peptides were purified by liquid chromatography using a Zorbax SB-C3 column (Agilent Technologies) with a reverse phase water (+ 0.05% TFA) / acetonitrile (+ 0.05% TFA) gradient and lyophilized. Mass spectrometry confirmed the molecular mass of the peptides.

Deuterated ethylene glycol (d6-EG), D_2O (99.9% D) (Cambridge Isotope Laboratories, Inc. Tewksbury, MA), phosphate buffered saline (PBS) (10X, Fisher Scientific), ethylene glycol (EG), triethylene glycol (TEG), poly(ethylene glycol) of MW 400 (PEG 400) (Fluka), and xylitol (Sigma-Aldrich) were used without further purification.

Osmolality

The osmolalities of the osmolyte solutions were determined as follows. Xylitol solutions were measured using a VAPRO model 5520 vapor pressure osmometer (Wescor, Logan, UT). Each xylitol solution was measured in triplicate, along with the no-osmolyte buffer, to obtain the osmolality at each concentration. TEG osmolalities were calculated using the equation: $[\mathrm{TEG}] = 1.0263m + 0.0291m^2$, where $m =$ molality,[29] and PEG 400 osmolalties were calculated using our previous equation.[30] EG and d6-EG osmolalities were taken as equal to their corresponding molalities.

Circular dichroism spectroscopy

CD spectra were collected with an RSM 1000 circular dichroism spectrophotometer using the Olis SpectralWorks software (Bogart, GA). Wavelength scans from 260 to 190 nm were performed with a 1 nm step resolution and integration time per data point determined automatically as a function of high volts. All CD experiments were conducted at 22°C. Aqueous solutions between 0.2 to 0.4 mg/mL of NCBD (= 30 to 60 μM) and ACTR (= 25 to 50 μM) in 1X PBS (pH 7.4) were prepared using MilliQ grade water. Peptide concentrations were determined by HPLC using a standard curve generated from amino acid analysis (AIBioTech, Richmond, VA). Samples were loaded into a 1 mm pathlength quartz cuvette. The CD spectrum of the corresponding buffer background, with the same osmolyte and osmolyte concentration, was subtracted from each sample spectrum. These background subtracted CD spectra were converted to units of mean residue ellipticity, $[\theta] = [\mathrm{deg\ cm^2 dmol^{-1}}]$. The helical fraction, f_h, was calculated from the equation

$$f_h = \frac{[\theta]_{222,meas} - [\theta]_{222,c}}{[\theta]_{222,h} - [\theta]_{222,c}} \tag{1}$$

where $[\theta]_{222,meas}$ is the measured mean residue ellipticity at 222 nm, and $[\theta]_{222,c} = 3000$ deg cm^2 dmol^{-1} and $[\theta]_{222,h} = -36,000$ deg cm^2 dmol^{-1} for a fully random coil and fully α-helical conformation, respectively.[31]

Osmotic stress thermodynamics

For a thermodynamic analysis of the coil-to-helix transition, f_h was normalized relative to the minimum and maximum α-helix for each IDP. Previous urea denaturation experiments on these IDPs showed $f_{\mathrm{h,min}} = 0$,[7] but neither NCBD nor ACTR is expected to reach 100% α-helix based on their sequence. Since an obvious $f_{\mathrm{h,max}}$ saturation point was not reached with any of the osmolytes measured, $f_{\mathrm{h,max}}$ was determined from sequence-based secondary structure propensity calculations.[32] The calculations yielded $f_{\mathrm{h,max}} = 0.576$ and 0.378 for NCBD and ACTR, respectively (see Figure S1). The relative $f_{h,rel} = f_h/f_{h,max}$, with f_h obtained by Equation 1, more appropriately reflects the actual range in secondary structure of each IDP. It should be noted that $f_{h,rel}$ also is directly obtained with Equation 1 by appropriately updating $[\theta]_{222,h}$. Then using the equilibrium constant between the folded and unfolded state, $K_{eq} = f_{h,rel}/(1 - f_{h,rel})$, the difference in the free energy change between water (ΔG_0) and and osmolyte (ΔG) is found: $\Delta\Delta G = -RT[\ln(K_{eq}) - \ln(K_{eq,0})]$, where $R =$ ideal gas constant and $T =$ temperature. The change in the number of preferentially hydrating water molecules associated with the transition (ΔN_w) is obtained with the linkage

$$\frac{\delta(\Delta\Delta G)}{\delta[Osm]} = RT\frac{\Delta N_w}{55.6} \tag{2}$$

where $[Osm] =$ osmolyte osmolality, and 55.6 = mol/kg water.[33]

This journal is © The Royal Society of Chemistry [year]

Small-angle neutron scattering

SANS experiments were performed on the extended Q-range small-angle neutron scattering (EQ-SANS) beam line at the Spallation Neutron Source (SNS) located at Oak Ridge National Laboratory (ORNL). In 60 Hz operation mode, a 2.5 m sample-to-detector distance with 2.5-6.4 $\AA$ wavelength band was used[34] to obtain the relevant wavevector transfer, $Q = 4\pi\sin(\theta)/\lambda$, where 2θ is the scattering angle. NCBD (2.4 mg/mL) samples were prepared in 1X PBS D_2O (pH measured, pH_m 7.4) and with 0, 10, and 20% (v/v) d6-EG. Peptide concentration was determined by UV-Vis using a calculated absorption, $A_{280}^{1mg/mL}$ = 0.228.[35] Samples were loaded into 2 mm pathlength circular-shaped quartz cuvettes (Hellma USA, Plainville, NY) and SANS measurements performed at 20°C. Data reduction followed standard procedures using MantidPlot.[36] The measured scattering intensity was corrected for the detector sensitivity and scattering contribution from the solvent and empty cells, and then placed on absolute scale using a calibrated standard.[37]

SANS analysis

Upon verifying a Guinier regime[38] in the SANS profiles, the pair distance distribution function, $P(r)$, was calculated from the scattering intensity, $I(Q)$, using the indirect Fourier transform method implemented in the GNOM program.[39] The $P(r)$ function was set to zero for $r = 0$ and $r = D_{\max}$, the maximum linear dimension of the scattering object. $D_{\max}$ was explored to optimize the $P(r)$ solution and excellent quality solutions were found in each case. The $P(r)$ solution to the scattering data yielded the real-space radius of gyration, R_g, and scattering intensity at zero angle, $I(0)$. The molecular mass, M, was calculated by

$$\frac{I(0)}{c} = \frac{M}{N_A}(\Delta\rho^2)\bar{\upsilon}^2 \quad (3)$$

where $\Delta\rho$ = contrast in scattering length density between protein and D_2O buffer solution ($= \rho_{\text{pro}} - \rho_{\text{buf}}$), $\bar{\upsilon}$ = protein partial specific volume (= 0.735 mL/g), and N_A is the Avogadro number. The protein scattering length density, ρ_{prot}, of NCBD ($= 3.075 \times 10^{10}$ cm^{-2}) was calculated from the sequence using the Contrast module of MULCh.[40] The D_2O scattering length density used was $D_2O = 6.388 \times 10^{10}$ cm^{-2}.

Results

IDP Secondary Structural Transitions with Osmotic Stress

We characterized the ability of NCBD and ACTR, two IDPs that are a known binding pair, to separately fold under osmotic stress conditions. Secondary structural changes in each unbound IDP were monitored by CD spectroscopy as various osmolytes were added to exert an osmotic stress. The osmolytes tested were a diol (EG), two polyether diols (TEG and PEG 400), and a polyol (xylitol). Both NCBD and ACTR gained α-helical content with increasing osmotic stress for all osmolytes measured, which parallels their folding upon NCBD/ACTR complex formation. The CD spectrum for NCBD in the absence of osmolyte shows a prominent negative peak at 222 nm, indicative of α-helix, and the spectra shift toward increasing α-helix with added PEG 400 (Figure 1A). The arrows in Figure 1A denote these changes, where the random coil signal ~200 nm diminishes and the α-helix signature at 222 nm becomes more pronounced. The CD spectrum for ACTR without any osmolyte shows mostly random coil. Like NCBD, ACTR also folds toward α-helix with the addition of PEG 400 (Figure 1B). We observed an isodichroic point around 205 nm for NCBD and ACTR with PEG 400, supporting a two-state transition from random coil to α-helix.

Using Equation 1, NCBD starts at 39% α-helix in the absence of osmolyte and reaches 54% α-helix in 40% (v/v)

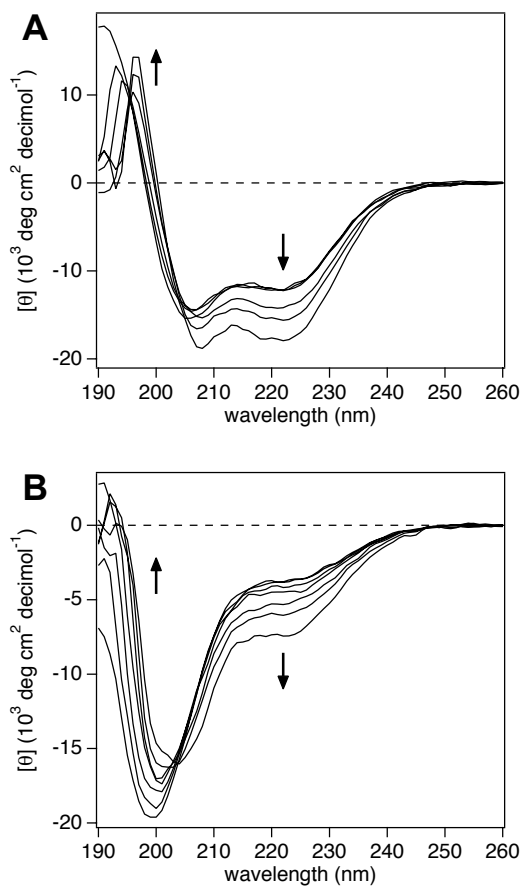

Fig. 1 CD spectra for (A) NCBD and (B) ACTR with added PEG 400. Increasing α-helical content is observed in both proteins with increasing PEG 400 concentration, from 0 to 40% (v/v) (indicated by the arrows).

PEG 400. ACTR, which has 17% α-helix without osmolyte, acquires 27% α-helix for the same PEG 400 concentration. To check for osmotic action and preferential interactions, we investigated the effects on IDP structure by additional osmolytes varying in size and chemistry. The CD spectra for NCBD with EG and TEG display a clear isodichroic point and show further helix formation with osmolyte addition (see Figure S2). For ACTR, the CD spectra with EG, xylitol, and TEG show helix formation with osmolyte addition (Figure S3). However, the CD curves for the higher osmolyte concentrations shift off of the 205 nm isodichroic point. Spectral deviations are noticed with EG and TEG at 30 and 40%, and xylitol at 3 and 4 molal (see Figure S3, *orange spectra*). These deviations could indicate intermediate states, an alternate folding pathway, or may result from protein-osmolyte interactions. We keep this in mind for the analysis below. The changes in $[\theta]_{222}$ with osmolality, for each IDP and osmolyte, are given in Figure S4.

Preferential Hydration Changes Accompanying Osmotic Folding

We quantified the osmotic folding energetics for NCBD and ACTR using the thermodynamics described in the Materials and Methods section. The NCBD CD spectra clearly showed a two-state transition with all osmolytes. Linear fits to the NCBD energy plots (Figure 2A) were suitable and with $\Delta\Delta G(0) \approx 0$ J/mol in each case. These osmolytes with NCBD therefore displayed osmotic effects. Using Equation 2, we quantified the net preferential hydration change accompanying folding, where $\Delta N_w < 0$ reflects water release. The resulting series, from least to greatest water release, followed: EG < TEG < PEG 400. Errors on ΔN_w values were $\approx \pm 1$. The osmolyte ordering also can be directly discerned from the $[\theta]_{222,h}$ vs. osmolality plots (see Figure S4A), where steeper slopes indicate more pronounced effects. The interpretation of the number of water molecules alternatively can be described by a preferential interaction coefficient[17] or m-value.[18] We maintain the osmotic stress framework here to focus on preferential hydration changes related to the observed structural transitions.

Linear slopes also were observed in the ACTR energy plots for each osmolyte tested (Figure 2B). The intercepts of the linear fits were inspected to discern if $\Delta\Delta G$ tended to 0 J/mol at 0 Osm, which would support an unchanged IDP initial state. Going from 0 to 0.85 Osm EG, there was a pronounced increase in the ACTR $\Delta\Delta G$. We repeated the EG measurements to verify the trend and obtained the same result (data included in Figure 2B). From 0.85 Osm and higher, ACTR with EG did display linearity with a negative slope, so we fit over this range to obtain an effective ΔN_w with $\Delta\Delta G(0) = 410 \pm 70$ J/mol. It is possible that protein-osmolyte interactions shift the energy plot, as discussed below. Fits to the other osmolytes had

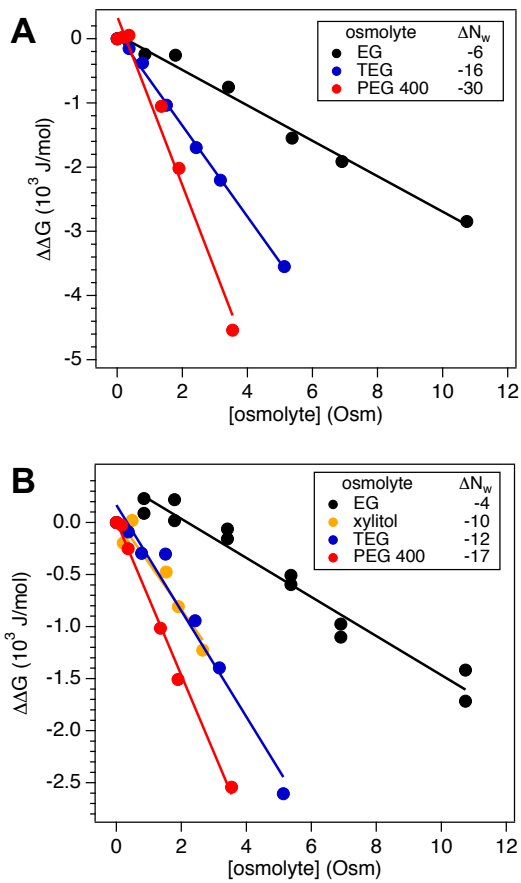

Fig. 2 (A) The change in NCBD folding free energy, $\Delta\Delta G$, with osmolality for EG, TEG, and PEG 400 yields the net hydration change, ΔN_w, accompanying folding, where $\Delta N_w < 0$ corresponds to water release (see legend for values). (B) The variation in ACTR $\Delta\Delta G$ for EG, xylitol, TEG, and PEG 400 provides ΔN_w accompanying osmotic folding (see legend for values).

$\Delta\Delta G(0) \approx 0$ J/mol, indicating the ACTR initial state is unaffected by these osmolytes. For the cases with CD isodichroic shifts at the highest osmolyte concentrations, we performed fits excluding these points in Figure 2B. The same ΔN_w and $\Delta\Delta G(0)$ for ACTR with EG was obtained. ACTR with xylitol and TEG only slightly differed from the original fits, yielding ΔN_w = -7 and -8, respectively. For ACTR, ordering the osmolytes by water release: EG < xylitol $\approx$ TEG < PEG 400. As mentioned for NCBD, the qualitative features for ACTR are also directly observable in the $[\theta]_{222,h}$ vs. osmolality plots (see Figure S4B). The trend in hydration changes for the diols is the same as observed for NCBD, with xylitol acting similar to TEG. However, it is important to remember in this comparison that ACTR experienced an altered initial state with EG.

A plot of ΔN_w vs. osmolyte molecular volume, v_m (Figure

This journal is © The Royal Society of Chemistry [year]

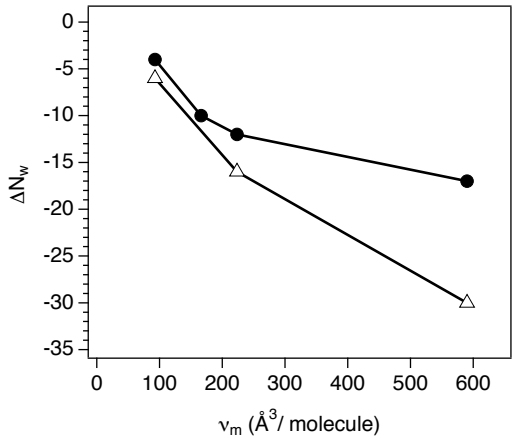

Fig. 3 Net hydration change, ΔN_w, accompanying the osmotic folding of NCBD (open triangles) and ACTR (filled circles) vs. molecular volume, v_m, of each osmolyte used (smallest to largest: EG, xylitol, TEG, and PEG 400).

3) was constructed to compare the osmolyte effects on the two IDPs. From the osmolyte molecular mass and density, the calculated $v_m = 93$, 166, 223, and 590 $Å^3$/molecule for EG, xylitol, TEG, and PEG 400, respectively. Both NCBD and ACTR show increasing water release with increasing osmolyte size. For any given osmolyte, the preferential hydration effects on NCBD were always larger than ACTR. Also, the difference between NCBD and ACTR ΔN_w increased with increasing v_m. It should be kept in mind that the absolute values of ΔN_w depend on our choice of helix propensity calculations (see Figure S1). However, the relative changes observed for each IDP with the osmolytes are independent.

NCBD Structural Changes with EG

To acquire further structural insight into the NCBD unbound state, we used SANS to measure the solution structure in the presence of deuterated EG (d6-EG). The d6-EG is contrast matched in 100% D_2O buffer to unambiguously resolve the protein structure. The variations in the SANS profiles for NCBD with increasing d6-EG concentration, from 0 to 20% (v/v), reflect protein conformational changes (Figure 4A). To quantify the structural changes and more carefully inspect protein shape, $P(r)$ functions for NCBD (Figure 4B) were calculated from the respective SANS profiles after first evaluating them with Guinier fits (Figure S5). The $I(0)$ and R_g values obtained from $P(r)$ analysis were consistent with those from the Guinier fits (Table 1).

Using Equation 3, the $I(0)$ values for NCBD in 0 to 20% d6-EG (Table 1) yield M from 6560 to 6980 Da, which are comparable to the actual 6545 Da. From the $P(r)$ values, the NCBD R_g decreased by $\sim$2 $Å$ with EG added up to 3.67 Osm

Table 1 SANS results for NCBD with ethylene glycol

	from Guinier		from $P(r)$		
% EG	$I(0)$ (cm^{-1})	R_g (Å)	$I(0)$ (cm^{-1})	R_g (Å)	D_{max} (Å)
0	0.0164(1)	14.8(2)	0.0165(1)	15.5(2)	55.0
10	0.0157(2)	14.0(3)	0.0155(2)	14.3(2)	47.7
20	0.0159(2)	13.5(2)	0.0156(1)	13.4(1)	42.0

(Figure 5). The maximum linear dimension, $D_{\max}$, of the protein also decreased by $\sim$13 $Å$ over this EG range (see Table 1). The $P(r)$ curve shapes illustrate a continual shift toward smaller intra-protein correlation distances with osmolyte addition. In particular, the $P(r)$ peak maximum shifts from 12.1 to 10.1 $Å$ between 0 and 1.63 Osm EG and remains at 10.1 $Å$ up to 3.67 Osm.

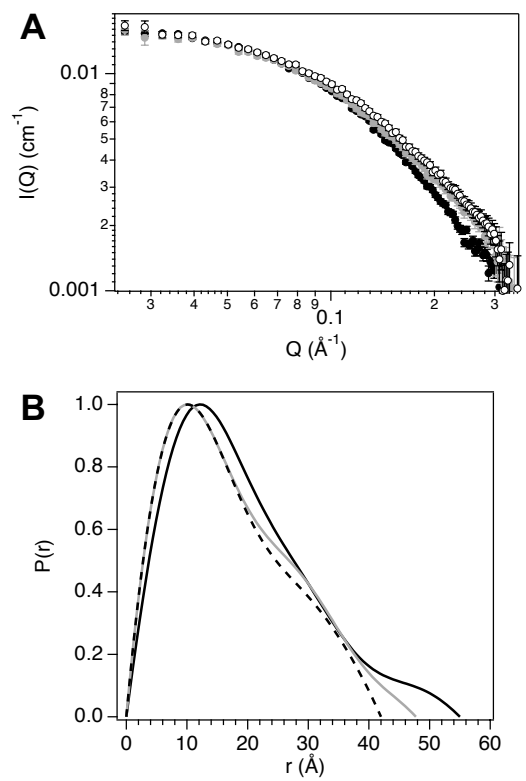

Fig. 4 (A) SANS curves, $I(Q)$ vs. Q, for NCBD with 0 (filled black circles), 1.63 (filled grey circles), and 3.67 Osm (open circles) d6-EG. (B) NCBD pair distance distribution, $P(r)$, curves for 0 (solid black line), 1.63 (solid grey line), and 3.67 Osm (dashed black line) d6-EG calculated from the scattering profiles.

To relate overall size changes with fraction helicity, first a sigmoid fit to the plot of NCBD f_h vs. [EG] (Figure S6) was performed to interpolate values. The NCBD R_g decrease, which is 14% overall, is substantial relative to the f_h increase

(Figure 5). The f_h change of ∼4% over this range corresponds to just ∼2 to 3 residues adopting an α-helical conformation. Therefore, the initial osmotic structural changes in NCBD appear to involve compaction in overall size with minimal gain in secondary structure.

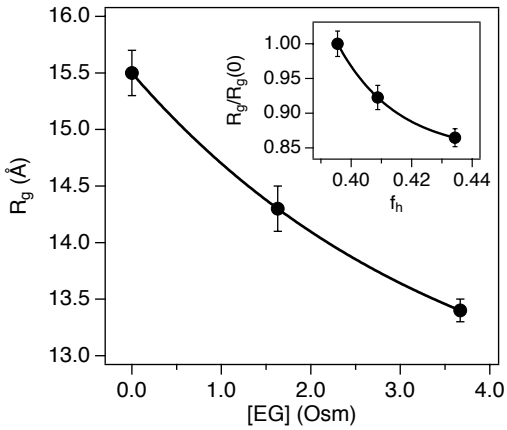

Fig. 5 NCBD R_g vs. EG osmolality. The inset shows the NCBD R_g normalized by the value at zero osmolyte, $R_g/R_g(0)$, vs. fraction helicity, f_h. Solid lines are exponential fits with an x-axis offset to guide the eye.

Discussion

Determining IDP transient, or preformed, structure and folding propensity is informative to delineate mechanisms for IDP folding-binding. Several studies on NCBD and ACTR have addressed aspects of conformational selection and binding-induced folding mechanisms.[41–45] A combination of these routes is generally believed to direct folding-binding. Kinetic experiments that modulated ACTR helix propensity with mutations were able to correlate greater ACTR helicity with stronger binding to NCBD.[28,45] Thus transient structure in the unbound state can poise ACTR for binding to NCBD. Some of these studies also tested TMAO effects on NCBD and ACTR.[41,42,44] TMAO acted to stabilize structures and was useful in discerning details about intermediate states along the NCBD/ACTR binding reaction.

In this study, the folding and preferential hydration properties of NCBD and ACTR were interrogated by osmotic stress. Although unbound NCBD is more folded than ACTR, both were equally responsive to osmotic folding. For example, going from 0 to the maximum EG concentration used in these experiments (40%), the calculated number of residues that adopt an α-helix was 6 for NCBD and 5 for ACTR. Similarly for TEG (from 0 to 40%), both IDPs had 7 residues adopt α-helix, and PEG 400 (from 0 to 40%) gave 9 for NCBD and 7 for ACTR. However, a key difference was NCBD always showed greater preferential hydration changes than ACTR for the same osmolyte (see Figure 3). This points to a greater importance of water for the NCBD conformational change.

Several different osmolytes were tested for comparison. The predominant effect on the IDPs was osmotic in driving a two-state transition from random coil to α-helix. The linearity in all of the energy plots (Figure 2) supports an osmotic, or water-mediated, structural transition in each case. However, a noticeable deviation was ACTR with EG, where the intercept, $\Delta\Delta G([osmolyte] = 0) > 0$ (see Fig. 2B). Direct EG interactions may change the ACTR initial state. Also for ACTR, we found a slight shift in the CD isodichroic point at the highest concentrations of EG, TEG, and xylitol. These shifts may indicate folding intermediates or an altered folding pathway. Again it is possible that protein-osmolyte interactions affect secondary structure at this point. Quantitative analysis with the osmotic stress method is most valid within the limit of low osmolyte concentrations. However, observing these subtle effects on ACTR may be instructive. For example, protein-PEG interactions have been shown to vary with PEG molecular mass, where chemical interactions are strongest for smaller PEG chains.[46] Our findings with ACTR appear consistent with this trend.

In general, with increasing osmolyte concentration, one can imagine a continuous reduction in available conformational space for an IDP. Alternatively, the IDP may be directed down an alternate set of conformations. The latter case was observed for α-synuclein, where the folding landscape with TMAO was different than driven by binding to SDS.[47] Since α-synuclein is aggregation prone, it could be more susceptible to finding an alternate pathway compared to many other IDPs. Still it highlights the potential for osmolyte-specific IDP ensembles. Another consideration is that IDP tertiary interactions become important during the osmolyte-driven compaction and folding process. Water structuring that helps mediate these tertiary interactions is certainly important. It may only be possible to fold at the secondary structure level up to a point without a binding partner, which could be the underlying reason for our observations with ACTR at highest osmolyte concentrations.

Osmolyte stabilizing and preferential hydration effects often increase with their size, mainly due to steric exclusion. Enthalpic contributions also should be considered, although they typically are not as dominant for polymeric crowders.[19,33] We found that NCBD and ACTR preferential hydration changes grew with increasing osmolyte size (see Figure 3). With a larger library of osmolytes, another osmotic stress study nicely demonstrates size-dependent effects on preferential hydration.[19] Also, PEG size-dependent effects on IDP conformation (including ACTR) were shown by single molecule FRET.[13] An important component in osmolyte-driven processes is the role of water. Osmotic stress analysis yielded wa-

This journal is © The Royal Society of Chemistry [year]

ter contributions, where NCBD preferential hydration changes always exceeded that for ACTR. Water restructuring at these protein interfaces likely governs their observed response to added osmolytes.

Last we correlated structural parameters obtained from SANS and CD for NCBD with EG. Initial compaction in shape was dramatic, as shown by the $P(r)$ curves (Figure 4B). Most prominent was the reduction in $D_{\max}$ from 55 to 42 $\AA$ over the [EG] range explored. By following the normalized $R_g/R_g(0)$ with f_h (Figure 5, inset), the 14% reduction in R_g is more than three-fold greater than the concomitant $\sim$4% gain in α-helicity. Therefore, the initial osmotic compaction of NCBD appears to involve only a modest gain in helical segments but likely generates more turns and loops that favorably assist in the overall size reduction observed from the R_g and $D_{\max}$.

In summary, we found new structural and hydration details concerning the intrinsic disorder of NCBD and its binding partner, ACTR. These IDPs provided a comparative study to gain insights into their folding propensity and preferential hydration changes with a variety of osmolytes. The results should assist in better discerning how IDP folding contributes to binding.

Acknowledgment

This research was supported by the U.S. Department of Energy, Office of Basic Energy Sciences through ORNL Laboratory Directed Research and Development grant 05246 (C.S.). A portion of this research was performed at Oak Ridge National Laboratory's Spallation Neutron Source, sponsored by the U.S. Department of Energy, Office of Basic Energy Sciences. We acknowledge laboratory support by the Center for Structural Molecular Biology, funded by the Office of Biological and Environmental Research of the U.S. Department of Energy.

References

1 V. N. Uversky, *Protein Science*, 2013, **22**, 693–724.
2 R. van der Lee, M. Buljan, B. Lang, R. J. Weatheritt, G. W. Daughdrill, A. K. Dunker, M. Fuxreiter, J. Gough, J. Gsponer, D. T. Jones, P. M. Kim, R. W. Kriwacki, C. J. Oldfield, R. V. Pappu, P. Tompa, V. N. Uversky, P. E. Wright and M. M. Babu, *Chemical Reviews*, 2014, **114**, 6589–6631.
3 P. E. Wright and H. J. Dyson, *Nat Rev Mol Cell Biol*, 2015, **16**, 18–29.
4 R. K. Das and R. V. Pappu, *Proc. Natl. Acad. Sci. USA*, 2013, **110**, 13392–13397.
5 M. R. Jensen, M. Zweckstetter, J. rong Huang and M. Blackledge, *Chemical Reviews*, 2014, **114**, 6632–6660.
6 E. B. Gibbs and S. A. Showalter, *Biochemistry*, 2015, **54**, 1314–1326.
7 S. J. Demarest, M. Martinez-Yamout, J. Chung, H. Chen, W. Xu, H. J. Dyson, R. M. Evans and P. E. Wright, *Nature*, 2002, **415**, 549–553.
8 P. E. Wright and H. J. Dyson, *Current Opinion in Structural Biology*, 2009, **19**, 31–38.
9 V. N. Uversky, *Biochimica et Biophysica Acta*, 2013, **1834**, 932–951.
10 I. M. Kuznetsova, K. K. Turoverov and V. N. Uversky, *International Journal of Molecular Sciences*, 2014, **15**, 23090.
11 I. V. Baskakov, R. Kumar, G. Srinivasan, Y.-s. Ji, D. W. Bolen and E. B. Thompson, *Journal of Biological Chemistry*, 1999, **274**, 10693–10696.
12 Y.-C. Chang and T. G. Oas, *Biochemistry*, 2010, **49**, 5086–5096.
13 A. Soranno, I. Koenig, M. B. Borgia, H. Hofmann, F. Zosel, D. Nettels and B. Schuler, *Proc. Natl. Acad. Sci. USA*, 2014, **111**, 4874–4879.
14 S. L. Flaugh and K. J. Lumb, *Biomacromolecules*, 2001, **2**, 538–540.
15 C. Szasz, A. Alexa, K. Toth, M. Rakacs, J. Langowski and P. Tompa, *Biochemistry*, 2011, **50**, 5834–5844.
16 D. P. Goldenberg and B. Argyle, *Biophysical Journal*, 2014, **106**, 905–914.
17 E. S. Courtenay, M. W. Capp, C. F. Anderson and M. T. Record, *Biochemistry*, 2000, **39**, 4455–4471.
18 M. Auton, D. Bolen and J. Rösgen, *Proteins*, 2008, **73**, 802–813.
19 S. Sukenik, L. Sapir and D. Harries, *Current Opinion in Colloid & Interface Science*, 2013, **18**, 495–501.
20 C. B. Stanley and H. H. Strey, *Biophysical Journal*, 2008, **94**, 4427–4434.
21 A. Badasyan, S. A. Tonoyan, A. Giacometti, R. Podgornik, V. A. Parsegian, Y. S. Mamasakhlisov and V. F. Morozov, *Phys. Rev. E*, 2014, **89**, 022723.
22 A. Badasyan, Y. S. Mamasakhlisov, R. Podgornik and V. A. Parsegian, *The Journal of chemical physics*, 2015, **143**, 014102.
23 H. Kang, P. A. Pincus, C. Hyeon and D. Thirumalai, *Phys. Rev. Lett.*, 2015, **114**, 068303.
24 S. Qin and H.-X. Zhou, *The Journal of Physical Chemistry Letters*, 2013, **4**, 3429–3434.
25 Y. C. Kim, A. Bhattacharya and J. Mittal, *The Journal of Physical Chemistry B*, 2014, **118**, 12621–12629.
26 M.-O. Ebert, S.-H. Bae, H. J. Dyson and P. E. Wright, *Biochemistry*, 2008, **47**, 1299–1308.
27 T. R. Keppel, B. A. Howard and D. D. Weis, *Biochemistry*, 2011, **50**, 8722–8732.
28 V. Iešmantavičius, M. R. Jensen, V. Ozenne, M. Blackledge, F. M. Poulsen and M. Kjaergaard, *Journal of the American Chemical Society*, 2013, **135**, 10155–10163.
29 *Laboratory of Physical and Structural Biology, Osmotic Stress*.
30 C. B. Stanley and H. H. Strey, *Macromolecules*, 2003, **36**, 6888–6893.
31 J. A. Morrow, M. L. Segall, S. Lund-Katz, M. C. Phillips, M. Knapp, B. Rupp and K. H. Weisgraber, *Biochemistry*, 2000, **39**, 11657–11666.
32 A. Drozdetskiy, C. Cole, J. Procter and G. Barton, *Nucleic acids research*, 2015, **43**, W389–W394.
33 R. Politi and D. Harries, *Chem. Commun.*, 2010, **46**, 6449–6451.
34 D. L. J. K. Zhao, C. Y. Gao, *Journal of Applied Crystallography*, 2010, **43**, 1068–1077.
35 E. Gasteiger, C. Hoogland, A. Gattiker, S. Duvaud, M. R. Wilkins, R. D. Appel and A. Bairoch, in *Protein Identification and Analysis Tools on the ExPASy Server*, ed. J. M. Walker, Humana Press, Totowa, NJ, 2005, pp. 571–607.
36 O. Arnold, J. Bilheux, J. Borreguero, A. Buts, S. Campbell, L. Chapon, M. Doucet, N. Draper, R. F. Leal, M. Gigg, V. Lynch, A. Markvardsen, D. Mikkelson, R. Mikkelson, R. Miller, K. Palmen, P. Parker, G. Passos, T. Perring, P. Peterson, S. Ren, M. Reuter, A. Savici, J. Taylor, R. Taylor, R. Tolchenov, W. Zhou and J. Zikovsky, *Nuclear Instruments and Methods in Physics Research Section A*, 2014, **764**, 156 – 166.
37 G. D. Wignall and F. S. Bates, *Journal of Applied Crystallography*, 1987, **20**, 28–40.
38 A. Guinier and G. Fournet, *Small-Angle Scattering of X-Rays*, Wiley, New York, 1955.
39 D. I. Svergun, *Journal of Applied Crystallography*, 1992, **25**, 495–503.
40 A. E. Whitten, S. Cai and J. Trewhella, *Journal of Applied Crystallogra-*

phy, 2008, **41**, 222–226.
41 M. Kjaergaard, K. Teilum and F. M. Poulsen, *Proc. Natl. Acad. Sci. USA*, 2010, **107**, 12535–12540.
42 J. Dogan, T. Schmidt, X. Mu, Å. Engström and P. Jemth, *Journal of Biological Chemistry*, 2012, **287**, 34316–34324.
43 M. Kjaergaard, L. Andersen, L. D. Nielsen and K. Teilum, *Biochemistry*, 2013, **52**, 1686–1693.
44 J. Dogan, X. Mu, Å. Engström and P. Jemth, *Scientific Reports*, 2013, **3**, 2076 EP –.
45 V. Iešmantavičius, J. Dogan, P. Jemth, K. Teilum and M. Kjaergaard, *Angewandte Chemie International Edition*, 2014, **53**, 1548–1551.
46 I. A. Shkel, D. Knowles and M. T. Record, *Biopolymers*, 2015, **103**, 517–527.
47 M. M. Moosa, A. C. M. Ferreon and A. A. Deniz, *ChemPhysChem*, 2015, **16**, 90–94.

This journal is © The Royal Society of Chemistry [year]